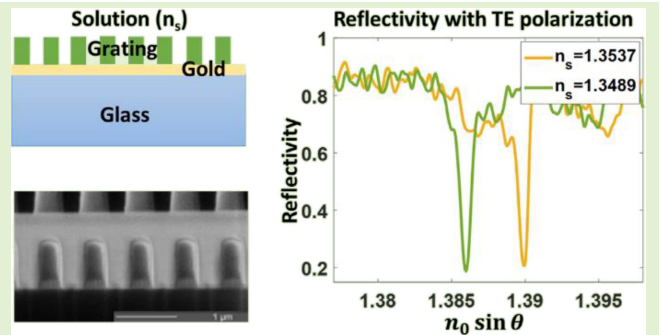


High Aspect-Ratio Open Grating Fabry-Perot Resonator for High-Sensitivity Refractive Index Sensing

Xiaoping Jiang¹, Mengqi Shen¹, Daniel Pak-Kong Lun², *Senior Member, IEEE*,
Wen Chen¹, *Senior Member, IEEE*, and Michael G. Somekh³

Abstract—This paper presents a high aspect-ratio open grating Fabry-Perot resonator theoretically and experimentally for aqueous refractive index sensing with high figure of merit. Transmission line modelling and associated Smith charts are utilized to give a better intuitive understanding of the physical sensing mechanism. The analysis aids understanding of the relative contribution to refractive index changes both within the grating fingers and external to them. Measurements of refractive index are carried out with Kretschmann coupling configuration for both transverse magnetic (TM) and transverse electric (TE) polarization. The results show an improvement of 10- and 44-fold in figure of merit over conventional SPR for TM and TE, respectively. When the designed system is analyzed for sensitivity, $1.874 \times 10^{-8} \text{ RIU}$ is achieved with a single frame even without a reference channel for noise cancellation. With 794 frames averaging (approximately 1-second acquisition time), the sensitivity of the system can be further improved to $1.609 \times 10^{-9} \text{ RIU}$. The simulations and experimental results demonstrate strong potential for biosensing applications, e.g., kinetic molecular binding, ultrasensitive refractive index sensing and photoacoustic detection.

Index Terms—Refractive index sensing, figure of merit, optical resonators.



I. INTRODUCTION

OPTICAL refractive index sensors have wide applications in many fields, e.g., biomedicine [1]–[5] and chemical analysis [6]–[9]. A prevalent operating principle uses an optical resonator which translates the changes in the environment to optical properties resulting in a change of resonance k -vector [10]. This change in resonance k -vector can be detected by the changes in the resonance angle or wavelength, as well as phase or intensity of the reflected light signal. The performance of the sensors can be evaluated by their bulk responsivity and figure of merit (FoM). Following Ref. [10], the term responsivity is used to refer to the change in the measured signal with a change of measurand, whereas we reserve the term sensitivity to refer to the detectable change of noise-equivalent refractive index unit (RIU). This term is therefore related to both the responsivity and the noise level. The effect of noise is discussed in Section III. D. Bulk responsivity and FoM are defined by

$$R_{\text{bulk}} = \frac{\Delta k_x / k_0}{\Delta n} \quad (1)$$

$$FOM = \frac{R_{\text{bulk}}}{FWHM} \quad (2)$$

Manuscript received 27 June 2022; accepted 29 June 2022. Date of publication 12 July 2022; date of current version 15 August 2022. This work was supported in part by the Science, Technology and Innovation Commission of Shenzhen Municipality under Grant KQTD20180412181324255; and in part by the Guangdong Provincial Pearl River Talents Program under Grant 2019JC01Y178. The associate editor coordinating the review of this article and approving it for publication was Prof. Carlos Marques. (Corresponding authors: Mengqi Shen; Michael G. Somekh.)

Xiaoping Jiang is with the Department of Electronic and Information Engineering, The Hong Kong Polytechnic University, Hong Kong, and also with the Shenzhen Key Laboratory of Micro-Scale Optical Information Technology, Nanophotonics Research Centre, Shenzhen University, Shenzhen, Guangdong 518060, China (e-mail: xiaoping.jiang@connect.polyu.hk).

Mengqi Shen is with the Shenzhen Key Laboratory of Micro-Scale Optical Information Technology, Nanophotonics Research Centre, Shenzhen University, Shenzhen, Guangdong 518060, China (e-mail: shen.mengqi@szu.edu.cn).

Daniel Pak-Kong Lun and Wen Chen are with the Department of Electronic and Information Engineering, The Hong Kong Polytechnic University, Hong Kong (e-mail: pak.kong.lun@polyu.edu.hk; owen.chen@polyu.edu.hk).

Michael G. Somekh is with the Shenzhen Key Laboratory of Micro-Scale Optical Information Technology, Nanophotonics Research Centre, Shenzhen University, Shenzhen, Guangdong 518060, China, and also with the Faculty of Engineering, University of Nottingham, Nottingham NG7 2RD, U.K. (e-mail: michael.somekh@nottingham.ac.uk).

Digital Object Identifier 10.1109/JSEN.2022.3188545

where $\Delta k_x/k_0$ denotes the normalized x -component of the wave vector, effectively $n_0 \sin \theta$, and FWHM denotes full width half maximum of a dip or a peak.

When a sensor measures the change in reflectivity, a higher FoM corresponds to a larger change of the reflected intensity for a given change in refractive index. Generally, high bulk responsivity R_{bulk} , narrow FWHM and high FoM are desired. Efforts have been made to increase the responsivity or narrow the FWHM with plasmonic sensors based on surface plasmon resonance (SPR) [2], [3], [6], long-range SPR [11], photonic sensors such as photonic crystal sensors based on Bloch surface waves [12] and whispering gallery mode sensors such as micro-ring resonators [13]. These approaches allow label-free detection of proteins, viruses and various molecules found in human body that are indicative in disease diagnosis and treatment with high precision and sensitivity [14]–[17]. However, for micro-ring resonators, the coupling configuration is somewhat complicated. For SPR and BSW sensors, they can be excited conveniently with attenuated total reflection (prism coupling) configuration, but a trade-off exists where a high-quality factor (Q) is associated with poor responsivity. This idea is encapsulated by the equivalent circuit model presented in [10] which shows that the analyte acts like an external load. This illustrates that strong coupling associated with good responsivity reduces the Q. Therefore, the overall FoM does not change a great deal [10], [12], so a sharp response is associated with a small change in the position of the resonance. The way to get around this trade-off is to design a resonator where the analyte is an intrinsic part of the resonator rather than just an external load.

With this consideration in mind, we established with rigorous coupled wave analysis (RCWA) simulations an open grating resonance structure [18] where an Fabry-Perot (FP) resonator was formed with the analyte and sub-wavelength grating between the gold layer and superstrate, and that the trade-off between Q and responsivity is broken. In the previous paper [18], it was demonstrated by simulation that good sensing performance could be achieved with high aspect ratio gratings. In the present paper, it is demonstrated that the approach is experimentally practicable with extreme sensitivity even with real world fabrication and material properties, so that inevitable imperfections in the fabrication still allow one to achieve performance that far exceeds that of other prism-based sensors. In addition to the experimental demonstration, a transmission line model and Smith chart give new physical insight into the performance of the structure, separating different mechanisms for high refractive index sensing. Despite concentrating on refractive index sensing, we also show that the structure is sensitive to analyte binding.

A high aspect-ratio sub-wavelength dielectric grating-based structure shown in Fig. 1 is demonstrated in both simulation and experiment exploiting both transverse magnetic (TM) and transverse electric (TE) polarization for refractive index sensing applications of aqueous solutions. The proposed structure uses a conventional prism (Kretschmann) configuration, the difference between the present structure and the conventional SPR is that the sensing structure consists of an open grating

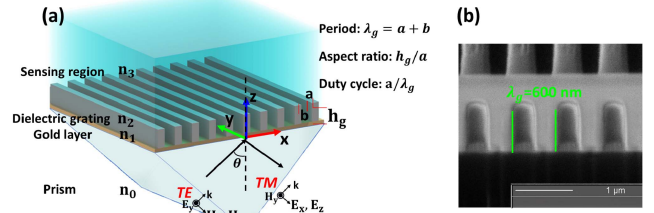


Fig. 1. (a) Diagram of the grating structure of Kretschmann configuration where λ_g is the grating period, a is width of the grating, b is the width between gratings and h_g is the height of the grating; (b) cross-section SEM image of a typical sample taken with a tilt of 45 degrees along the vertical direction; period of the grating is 600nm. The sample was produced with FIB and platinum was coated beforehand to increase conductivity contrast. Note that the 45-degree tilt results in a foreshortening by a factor of approximately $\sqrt{2}$ so the true height of the grating is $\sim 1 \mu\text{m}$.

resonator rather than simply a metal layer. In order to benchmark the performance of the proposed resonator, an SPR sensor with a 48 nm Au layer is also tested in the same experimental system for comparison.

The ability to compare a conventional SPR measurement against the current system using the same optical configuration removes bias due the optical system and allows more direct comparison of the sensing structures.

The 48 nm Au layer, which provides the optimum FoM with a gold based SPR sensor at 633 nm wavelength, was coated on top of coverslip by a sputterer (Nano 36, Lesker JLC). It is reasonable to choose conventional SPR as reference since its performance is well established and the comparison can be drawn within the same system [19]. The experimental FoM shows over 44-fold improvement over conventional SPR. Since the experimental coupling configuration is the same as conventional prism based Kretschmann configuration, the designed structure also has excellent potential for biosensing. This work also develops an intuitive picture of the system by looking at the field distribution in the structure as well as a Smith chart representation of the analyte detection, which helps visualization of the different detection mechanisms.

This paper is divided into four parts, Section II provides an intuitive explanation of the physical mechanism with transmission line model for layer-wise analysis and Smith chart for responsivity analysis. Section III presents and discusses the experiment data of the proposed sensor with TE and TM polarization with comparison to SPR sensing. Section IV draws a conclusion.

II. EXPLANATION OF THE PHYSICAL MECHANISM

The structure studied here is an open grating sensor consisting of a gold layer and a grating layer as shown in Fig. 1 with incident light of TM and TE polarization, respectively. The sensor features a grating layer of 1 μm height, 600 nm period and 240 nm grating width. This section will use transmission line model and Smith chart to give some new insight into the performance of the structure to explain the layer-wise physical mechanism and discuss the in-grating responsivity and out-

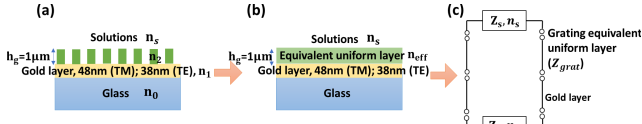


Fig. 2. (a) The high aspect ratio grating structure; (b) structure with equivalent uniform layer approximation; (c) transmission line model of the high aspect ratio grating structure.

grating responsivity. We emphasize that the transmission line model is used to develop intuition, it is always compared with RCWA for validation.

A. Transmission Line Model and Effect of the Grating Layer

Under certain conditions (essentially the structure supports a single dominant Bloch mode inside the grating layer [20]), simulations can be simplified by modelling the grating layer as an equivalent uniform layer with an effective refractive index (n_{eff}), this is the regime where effective medium theory is valid; the range of validity for the present structure was further discussed in [18]. With the effective medium approximation, all layers inside the structure can be considered homogeneous and their characteristic impedance for TM and TE polarization are given by [21]

$$Z_{TM} = \sqrt{\frac{\mu_0}{\epsilon}} \cos \theta, Z_{TE} = \sqrt{\frac{\mu_0}{\epsilon}} \frac{1}{\cos \theta} \quad (3)$$

The equivalent transmission line circuit of the structure can be applied to gain some insight. Figs. 2(a)-2(c) show the schematics of the structure, its equivalent structure and equivalent transmission line circuit. It can be seen from Fig. 2(b) that an FP cavity is formed in the equivalent uniform layer (green) between the gold layer and the solutions.

Effective medium approximation is applied to calculate the effective permittivity ϵ_{eff} and effective refractive index n_{eff} of the grating layer. To obtain n_{eff} we applied a Maxwell-Garnett model [22], [23] which provides better agreement with RCWA than a simple weighted average of permittivity [18]. The effective permittivity ϵ_{eff} and effective refractive index n_{eff} are given by

$$\epsilon_{eff} = \epsilon_g \frac{(\epsilon_s + 2\epsilon_g) + 2f(\epsilon_s - \epsilon_g)}{(\epsilon_s + 2\epsilon_g) - f(\epsilon_s - \epsilon_g)} \quad (4)$$

$$n_{eff} = \sqrt{\epsilon_{eff}} \quad (5)$$

where ϵ_s is the permittivity of the solution, ϵ_g is the permittivity of the grating.

It can be seen from the equivalent structure and transmission line model that a FP cavity is formed between the gold layer and the external solution. A crucial difference between the present sensor over, say, an SPR sensor is both the change of Z_{grat} and Z_s affect the response in the grating whereas in the SPR system only Z_s changes. Since the grating region is sufficiently thick to form a resonator, this amplifies any changes in Z_s .

In this section, as shown in Eq. (1), measurement of FWHM and calculation of FoM are based on $n_0 \sin \theta$ rather than θ , since $n_0 \sin \theta$ is proportional to k_x . Therefore, the unit of FWHM is the same of $n_0 \sin \theta$, that of the bulk responsivity

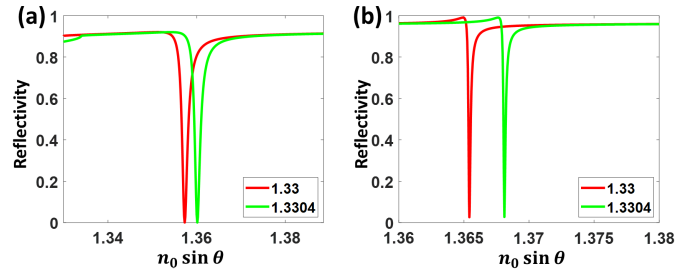


Fig. 3. The typical response of the high aspect-ratio open grating sensor with (a) TM and (b) TE polarization where red curve represents the solution of refractive index of 1.33 and green curve represents the solution of refractive index of 1.3304.

R_{bulk} is RIU^{-1} , and that of the FoM is RIU^{-1} . The choice of $n_0 \sin \theta$ is also appropriate because it is almost independent of the choice of prism material (n_0).

B. Effect of the Metal Layer

The structure studied here is an open grating sensor consisting of a gold layer and a grating layer. The sensor features a 48 nm gold layer for TM modes and 38 nm for TE modes functioning as a coupling layer to the grating. The value is determined by simulation with the aim of optimizing the FoM, being a compromise between coupling to the grating resonator and its Q. Although the thickness of the gold layer used for the TM mode is similar to the optimum value used surface plasmon resonance sensors at the same wavelength, the resonant angle does not correspond to strong excitation of surface plasmons, and the gold layer acts as a lossy mirror in a FP resonator for both TM and TE polarization. The loss in the metal means that there is a reflectivity minimum when the resonant conditions are met. It can be seen from Fig. 3 that clearly resonance mode of TM light exhibits a broader FWHM compared with that of the TE light, and this can be explained in terms of loss in the metal layer. It may be readily verified that the absorption loss for TM polarization is always greater than for TE polarization; this effect is even more pronounced when one factors in that the optimum thickness for TE is less than that for TM. The simulations of Fig. 3 show a reflectivity minimum of 48nm and 38nm for TM and TE, respectively. The resonance is much sharper for TE polarization.

C. Overall Performance

In a transmission line circuit, structure reactance X_s and structure resistance R_s are two factors affecting the resonance. The resonance condition is satisfied when the reactance in the circuit is cancelled out, which is $X_s = 0$, and thus k_x is real. At the resonance position, the full width half maximum (FWHM) of the dip is described by [10]

$$\Delta k_x = 2(dk_x / dX_s) R_s \big|_{k_x = k_{sp}} \quad (6)$$

The Q factor is given by

$$Q = \frac{k_{sp} \frac{dX_s}{dk_x}}{2R_s} \quad (7)$$

TABLE I
A COMPARISON BETWEEN SPR, TM AND TE

TL model	FOM = $\frac{dX_s}{dn_s} \frac{1}{2R_s} \big _{k_x=k_{sp}}$				Q factor
	dX_s/dn_s	R_s	FOM	Q = $k_{sp} \frac{dX_s}{dk_x} / 2R_s$	
	SPR	1.88	0.03	31.33	33.19
RCWA Analysis	Grating TM	12.48	0.014	445.71	908
	Grating TE	292.31	0.053	2757.64	6159
	FOM = $\frac{dk_x}{dn_s} / \Delta k_x$				Q factor
RCWA Analysis	$\frac{\Delta k_x/k_0}{\Delta n_s}$	FWHM ($\Delta k_x/k_0$)	FOM	Q = $k_{sp} / \Delta k_x$	
	SPR	1.155	3.548×10^{-2}	32.57	36.51
	Grating TM	0.6807	1.55×10^{-3}	439.40	881.46
RCWA Analysis	Grating TE	0.6269	2.26×10^{-4}	2763.11	6072.67

FOM is calculated at $n_s = 1.33$.

Therefore, the FoM can be expressed as

$$FoM = \frac{dk_x}{dn_s} = \frac{\frac{dk_x}{dX_s} \frac{dX_s}{dn_s}}{2(dk_x/dX_s)R_s} = \frac{dX_s}{dn_s} \frac{1}{2R_s} \big|_{k_x=k_{sp,o}} \quad (8)$$

In this study, the Q factor and the FoM of the resonance are calculated with a transmission line model. And the results are compared with RCWA to verify the model. Table I shows a comparison of FoM and Q factor between SPR, TM and TE grating samples calculated by both transmission line model and RCWA. Since the circuit parameters are not available with RCWA, the FoM and the Q factor are calculated directly. FWHM of the TM dip is approximately 1/23 of SPR dip, while for the TE mode, it is 1/157. There is an excellent agreement between the transmission line model and the RCWA, showing that for this structure the effective medium is a good approximation.

Table I shows a comparison between the FoM and Q using both transmission line modelling and RCWA. The agreement is particular satisfying as the circuit parameters are not accessible in the RCWA model so direct measures from the reflectivity curves are used. The circuit parameters show that the high FoM and Q of the TE mode is associated with the large change in reactance with analyte index; this is, in turn, directly related to the stored energy in the cavity. This difference in energy storage with TE and TM also apparent in Fig. 4 where the enhancement of the transverse field is considerably larger for TE compared to TM. Both TE and TM have much larger field enhancement compared to SPR. Finally, it is worth pointing out that with the grating structures the field peaks within the grating fingers accounting for the high FoM for refractive index, there is still a considerable field emerging beyond the fingers in the region of the external analyte, for TE mode the

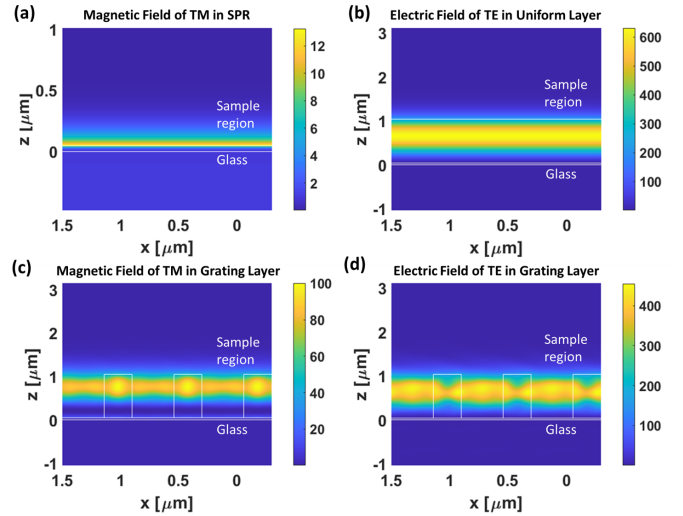


Fig. 4. In-resonance field distribution of (a) SPR, (b) TE with uniform grating layer, (c) TM mode with grating layer and (d) TE mode with grating layer.

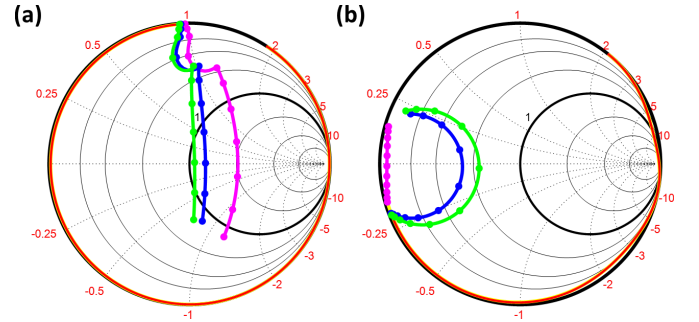


Fig. 5. The Smith chart showing the sensing process of the high aspect-ratio grating based sensor with (a) TM and (b) TE polarization. The orange curves that approximately follow the circumference represent the changing reflection as the grating thickness is increased to 1 mm, and the metal layer is then inserted between the grating and the incident light. The thickness of the gold layer varying from 0 to 60 nm with a step of 6 nm (shown with the dots) and change of refractive index from 1.33 (green solid line) to 1.3304 (magenta solid line), whereas blue solid line represents the situation where refractive index of the grating layer is not modulated and the index of the superstrate is 1.3304.

field enhancement at the interface between the fingers and the sample region is approximately 160.

D. In-Grating Responsivity and Out-Grating Responsivity

In Figs. 4(b)-4(d), the peak field enhancement arises within the grating and the Smith chart representation separate the contributions due to changes of refractive index with the grating and changes in the sample region. The Smith chart allows the phase and amplitude changes in reflectivity to be easily visualized since the distance from the origin of the chart represents the modulus of the reflectivity and the angular direction shows the reflectivity phase.

The total responsivity of TM modes is examined first. In the simulation, 240 nm wide grating with refractive index of 1.49 (effectively PMMA) and period of 600 nm are used. The sensing process is described in terms of the Smith chart in Fig. 5(a), which shows the change in reflectivity as the sample is built from the sample region of Fig. 2(b). The process starts with a pure grating with thickness increasing from 0 up to 1 μm , shown as the orange curve moving approximately

around the circumference of the circle. It should be noted that the gold layer with thickness from 1 to 60 nm is inserted as a coupling layer to modulate the reflectivity to make the reflected intensity vary close to resonance. As the incident angle is beyond the critical angle, the reflectivity is close to 1 when there is no gold layer. It should be noted that these calculations were performed with RCWA, so that the small deviation of the actual reflectivity from the circumference of the chart (unit reflectivity) is caused by grating diffraction scattering into propagating modes. The structure was filled with analyte with refractive index of 1.33 which is then increased by 4×10^{-4} to 1.3304. The green curve marks the refractive index of the analyte being 1.33 and magenta 1.3304. The spots on the line represent changes in gold thickness of 6 nm starting from 0 nm to the last point of 60 nm. The optimum thickness for reflectivity change with refractive index was 48 nm. With grating of $1 \mu\text{m}$ thickness, the FWHM is 1.550×10^{-3} and bulk responsivity is $0.6807 RIU^{-1}$. The FoM is $439.4 RIU^{-1}$.

Responsivity to material outside grating may also be investigated with this model, where the refractive index between the grating fingers is 1.33 and not changed whereas the refractive index outside the grating layer is changed from 1.33 to 1.3304. The result is shown as the blue path in Fig. 5(a). The signal change is reduced to 25%, but there is still substantial responsivity even if the impedance of the grating layer does not change. This indicates that approximately 75% of the refractive index sensitivity arises from perturbation inside the grating and the rest from the external perturbation. The FWHM is 1.550×10^{-3} and bulk responsivity is $0.1512 RIU^{-1}$. The FoM is 112, which is still considerably greater than FoM associated with SPR. This indicates that even a homogeneous layer can form an effective sensor to detect, say, protein binding. The reduced but still substantial sensitivity to out of grating changes in index is consistent with the field diagrams of Fig. 4 where despite a peak field inside the grating there is still considerable leakage into the sample region. Although the change of the grating impedance is the key mechanism conferring refractive index responsivity on this structure, the response to changes outside the grating is significant. At first sight this responsivity may seem a little counter-intuitive since total internal reflection gives a large reflection at the grating sample interface regardless of the sample refractive index, however, examination of the structure shows that the phase of the reflection at the grating/sample interface is sensitive to the refractive index of the sample medium even above the critical angle, thus changing the resonant k -vector determined by the transverse resonance condition.

For TE incident polarization we can follow the same process as the TM case. In Fig. 5(b), the green line stands for the reflectivity with refractive index of 1.33. The magenta line stands for the reflectivity with refractive index of 1.3304. The blue line stands for the reflectivity with a constant grating and sample refractive index of 1.3304, showing the dominant effect of the internal perturbation compared to the external perturbation. For TE, the FWHM is 2.269×10^{-4} and bulk responsivity is $0.6269 RIU^{-1}$. The FoM with changing impedance in the grating is $2763 RIU^{-1}$. For a constant

TABLE II
COMPARISON OF FOM FOR LAYER BINDING BETWEEN SPR, TM AND TE

Thickness	SPR	TM	TE
10 nm	4.4	7.40	20.9
100 nm	21	37	172
200 nm	25	66	271
400 nm	29	89	349

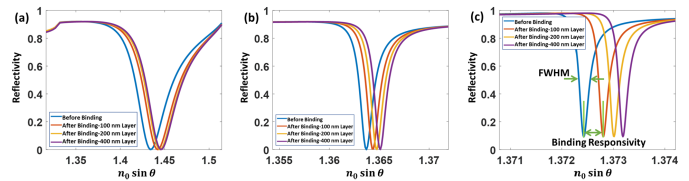


Fig. 6. Reflectivity of (a) conventional SPR, (b) TM and (c) TE mode of grating structure with a thin layer binding analysis. In the plot, blue curves mark the reflectivity before the binding, orange curves mark the reflectivity after binding with a 100-nm binding layer, yellow curves mark the reflectivity after binding with a 200-nm binding layer and violet curves mark the reflectivity after binding with a 400-nm binding layer.

grating, it is $376 RIU^{-1}$, which is a still 12-fold improvement over the SPR value.

Thus, we can safely say that the energy stored within the grating layer provided the majority of the responsivity, but the energy outside the grating layer provides substantial out-grating responsivity, by a factor of 4 for TM polarization and 12 for TE.

E. Binding Sensitivity Analysis

It has been established that, for high aspect ratio open grating structure, FoM and bulk responsivity come both from within and outside the grating, a binding analysis is presented in this subsection. The analysis again uses a conventional SPR as a benchmark. In this analysis, a fixed grating made from refractive index contrast of 1.49 and 1.33 is adopted where refractive index in the grating layer is not modulated. By analogy with the CM5 chips used in Biacore 3000, where a 100 to 200-nm thick dextran layer is formed on top of the gold film as the binding layer [24], a binding layer of 10 nm, 100 nm, 200 nm and 400 nm are simulated on top of the structure with a refractive index of 1.33 and 1.34 before and after the binding, respectively. Above the binding layer is aqueous solution with a constant refractive index of 1.33. Reflectivity for 100-nm, 200-nm and 400-nm binding layer are shown in Fig. 6(a)-6(c) for SPR, TM and TE respectively. Calculated FoM are shown in Table II.

TM and TE modes exhibit a 2-fold and 5-fold improvement over conventional SPR in 10-nm thick binding layer analysis, a 2-fold and 8-fold improvement over conventional SPR in 100-nm thick binding layer analysis, a 2.5-fold and 11-fold improvement over conventional SPR in 200-nm thick binding layer analysis and a 3-fold and 12-fold improvement over

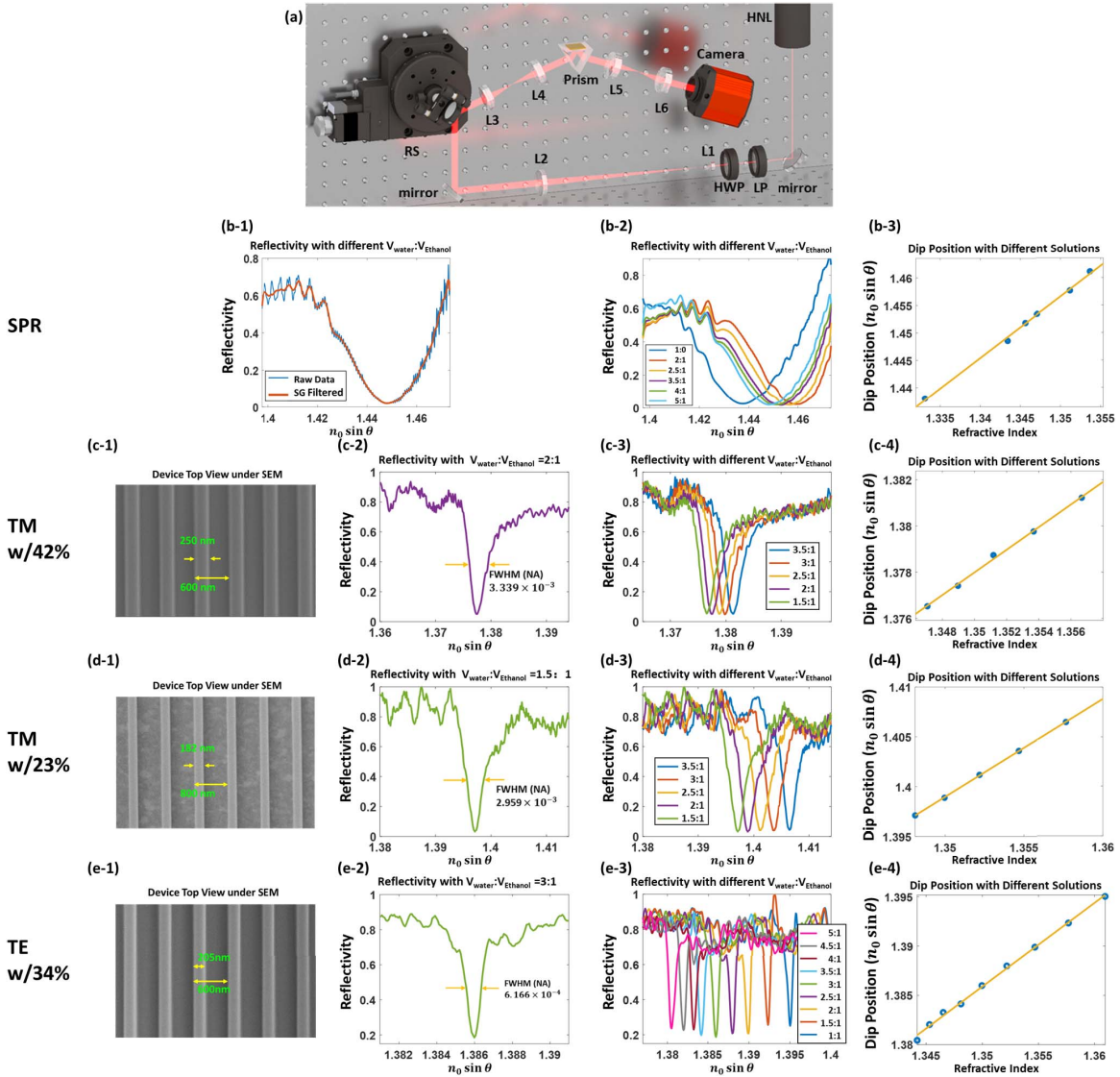


Fig. 7. (a) Schematics of the system. HNL: Linearly Polarized He-Ne Laser at 633 nm wavelength; LP: Linear Polarizer, HWP: Half Waveplate at 633nm; L1-L6: achromatic lenses; RS: motorized Rotation stage synced with camera by a computer. (b) Results from conventional SPR sample: (b-1) Reflectivity of a SPR sample and its SG filtered data, (b-2) reflectivity of the SPR sample with different aqueous solutions, (b-3) dip positions extracted from reflectivity and their linear regression. (c) Results from the TM sample with 42% duty cycle: (c-1) top-view SEM image, (c-2) reflectivity with $V_{\text{water}}:V_{\text{ethanol}} = 2:1$, (c-3) reflectivity with different aqueous solutions and (c-4) dip position and their linear regression. (d) Results from the TM sample with 23% duty cycle: (d-1) top-view SEM image, (d-2) reflectivity with $V_{\text{water}}:V_{\text{ethanol}} = 1.5:1$, (d-3) reflectivity with different aqueous solutions and (d-4) dip position and their linear regression. (e) Results from the TE sample: (e-1) top-view SEM image, (e-2) reflectivity with $V_{\text{water}}:V_{\text{ethanol}} = 3:1$, (e-3) reflectivity with different aqueous solutions and (e-4) dip position and their linear regression.

conventional SPR in 400-nm thick binding layer analysis. The results demonstrate the structure is superior for the detection of changes outside the grating compared to SPR. Since the evanescent field from the grating extends further than the surface plasmon field the advantage is smaller for the thinner layers. For binding of large molecules such as cell, spores and bacteria, e.g., a thicker binding layer, the performance will tend to the results in the last row of Table II.

III. RESULTS AND DISCUSSION

A. System Configuration

The experimental setup consists of an angle scanning configuration based on a rotating mirror as shown in Fig. 7(a). A prism (BK-7, OPRE32-22, Zolix) is chosen to excite the

modes beyond the critical angle. There are three pairs of lenses inside the system for beam expansion, mode excitation and beam collection, respectively. A linearly polarized He-Ne laser operating at the wavelength of 633 nm (33091, REO) was chosen as the laser source. After the linear polarizer (LPVIS100-MP2, Thorlabs), the beam was modulated by a half waveplate and expanded 13 times by lens L1 ($f=15$ mm, Thorlabs) and L2 ($f=200$ mm, Thorlabs). After L2, in the light path at the focal length of L2 and L3, a silver mirror (PF10-03-P01, Thorlabs) is mounted onto a motorized rotation stage (HDR50/M, Thorlabs). The beam was then projected onto the sample above the equilateral prism with lens L3 and L4. Lenses L5 and L6 are used to collect the reflected beam to be projected onto the camera (DCC3240/M, Thorlabs).

Lenses L3-L6 are achromatic lenses with a focal length of 50mm. The camera, the samples and the silver mirror on the rotation mount are on the conjugate plane to each other to reduce the movement of the illuminated area on the camera.

In order to validate the performance of the system we chose to use an angle scanning configuration where the reflected light was detected with a camera. In a practical sensor system, it is usually more convenient to use incident light with a range of incident angles and a line scan detector to capture all incident angles in a single shot. In our validation experiments, however, this was not appropriate as we compared modes with angular ranges that differed over nearly two orders of magnitude so that a single angle range could not be used without a complete change of the optical system. Utilization of a camera for detection combined with integration over several pixels proved useful as it enabled one to monitor the quality of the returning optical beam. Switching between TM and TE polarizations was implemented with a half wave plate.

To examine the FoM, ethanol and de-ionized (DI) water were mixed with different mixture ratios prior to deposition on the structures and refractive index of each solution was measured with an Ellipsometer (UVISSEL Plus, Horiba). The image acquisition sequence was developed with Python 3.6 which allows a fine control over the stage and camera simultaneously. In the experiments with the SPR samples and TM samples, the angular increment applied to the stage was set to 0.01° while that of TE samples was 0.005° . The total acquisition time was less than a minute for 400 steps. A typical acquired image sequence could be found in APPENDIX A. In data presentation, the reflectivity is plotted against $n_0 \sin \theta$ rather than θ since this parameter is almost independent of the material of the coupling layer.

B. SPR Results

The SPR samples were measured first as a reference to study the performance of TM and TE modes in the high aspect-ratio grating based sensors. SPR samples used in the experiment consist of 2 nm Cr and 48 nm Au, manufactured with the sputtering system (Nano 36, Lesker JLC). The results were acquired by measuring the reflectivity curves for each solution. For the SPR sample, FWHM of the resonance dip is relatively wide, and in the experimental system, the rotation stage gave fine control over angle increments of 0.01° . A 3-order Savitzky-Golay filter [25] with a window of 31 points to filter out the effect of parasitic interference in the optical path. The dip position ($n_0 \sin \theta$) as well as its FWHM as shown in Fig. 7(b-1). The dip positions of different solutions retrieved from Fig. 7(b-2) are marked with respect to solution refractive indices in Fig. 7(b-3). Then, a linear regression was performed, and its slope is the bulk responsivity $\frac{dn_0 \sin \theta}{dn_{\text{solution}}}$. The bulk responsivity retrieved from SPR samples was $1.100 RIU^{-1}$, and the FWHM was 0.03458 in $n_0 \sin \theta$. Thus, the FoM was $31.8 RIU^{-1}$.

C. TM and TE Mode Results

Samples were manufactured by the sputtering system (Nano 36, Lesker JLC) for 2 nm Cr and 48 nm Au and electron

beam lithography (EBPG 5150, Raith BV) for the grating. The detailed procedure of sample preparation could be found in APPENDIX B. The measurement procedures are similar to those for conventional SPR samples. A major difference is $n_0 \sin \theta$ associated with the modes. For conventional SPR with 2 nm Cr and 48 nm Au, the value of $n_0 \sin \theta$ associated with the mode varies between 1.44 and 1.47 in this experiment, which for this experiment is 0.11 higher than the critical angle. With a layer of grating, the TM and TE modes were excited from values of 1.34 in $n_0 \sin \theta$, which is only slightly higher than the critical angle, which gives a larger range of excitation k -vector and a larger dynamic range. The volume mixture ratios used were 2.5:1, 3:1, 3.5:1, 4:1 and 4.5:1. As described in Eqs. (1) and (2), the fill factor (duty cycle) determines effectiveness of the internal perturbation thus affecting the bulk responsivity. Two sets of TM samples with different grating duty cycles were prepared and investigated. Their results are shown in Figs. 7(c) and 7(d).

The first set had a duty cycle of 42%. The profile of the grating is 250 nm in width and 600 nm in period measured from the top view of the grating profile under SEM in Fig. 7(c-1). In Fig. 7(c-2), the FWHM is 3.339×10^{-3} in $n_0 \sin \theta$. Fig. 7(c-3) shows the reflectivity of all tested solutions to retrieve all the dip positions. Dip positions of solutions with respect to the refractive indices are shown in Fig. 7(c-4) with the linear regression to show the bulk responsivity $\frac{dn_0 \sin \theta}{dn_{\text{solution}}}$ of $0.4896 RIU^{-1}$. Therefore, the FoM was $147 RIU^{-1}$, which is 4.7 times higher than that of the conventional SPR sample.

The second set has a duty cycle of 23%. The profile of the grating is 182 nm in width and 800 nm in period measured from the top view of the grating profile under SEM shown in Fig. 7(d-1). Measured from reflectivity in Fig. 7(d-2), FWHM is 2.959×10^{-3} in $n_0 \sin \theta$, 11.5% narrower than that of 42% duty-cycle samples. Fig. 7(d-3) shows the reflectivity of all tested solutions to retrieve all the dip positions. Dip positions of solutions with respect to the refractive indices are shown in Fig. 7(d-4) with the linear regression to show the bulk responsivity $\frac{dn_0 \sin \theta}{dn_{\text{solution}}}$ of $0.9809 RIU^{-1}$. Therefore, the FoM was $331 RIU^{-1}$, a 10-fold improvement over the conventional SPR sample. These experiments indicate that for TM polarization the decrease in duty cycle results in narrow FWHM and high bulk responsivity with a corresponding increase in FoM.

For TE samples, 2 nm Cr and 38 nm Au were deposited by the sputtering system and grating fabricated by EBPG 5150 (Raith BV). The volume mixture ratios of water and ethanol used are 1:1, 1.5:1, 2:1, 2.5:1, 3:1, 3.5:1, 4:1, 4.5:1 and 5:1. The angular increment of the rotation motor used was 0.005° as the FWHM of the TE mode is considerably smaller than that of the TM mode and conventional SPR.

The width of the grating is 205 nm, and the period is 600 nm as measured from the top view of the grating profile under SEM in Fig. 7(e-1). The FWHM of reflectivity with 3:1 mixture ratio of water and ethanol measured from the curve in Fig. 7(e-2) is 6.166×10^{-4} in $n_0 \sin \theta$. The reflectivity of solutions with different mix ratios is shown in Fig. 7(e-3). Compared with conventional SPR, the FWHM

TABLE III
COMPARISON BETWEEN TM, TE AND CONVENTIONAL SPR

	Bulk Responsivity (RIU^{-1})	FWHM	FoM (RIU^{-1})
TM w/ 42% duty cycle	0.4986	3.339×10^{-3}	147
TM w/ 23% duty cycle	0.9809	2.959×10^{-3}	331
TE w/ 35% duty cycle	0.8598	6.166×10^{-4}	1394
Conventional SPR	1.100	3.458×10^{-2}	31.8

is improved by a factor of 56, and compared with TM it is improved by a factor of 5. Dip position retrieved is marked in Fig. 7(e-4) together with its linear regression showing the bulk responsivity of $0.8598 RIU^{-1}$. Therefore, the measured FoM was $1394 RIU^{-1}$, a 44-fold improvement over that of conventional SPR acquired in the same system and over 4-fold improvement over that of the TM grating samples.

The results of TM and TE grating samples together with the conventional SPR sample are summarized in Table III.

D. Sensitivity Analysis

The sensitivity of a refractive index sensing system is equivalent to the minimum detectable change of sample refractive index and is determined by noise level, bulk responsivity and slope of the reflectivity curve, which is related to the FWHM and dip prominence. It is described by

$$\Delta n = NEP / \left(\frac{dI}{dn_0 \sin \theta} \cdot \frac{dn_0 \sin \theta}{dn_s} \right) \quad (9)$$

where Δn denotes the sensitivity of the system, NEP denotes the system noise level, $\frac{dI}{dn_0 \sin \theta}$ denotes the slope of the reflectivity and $\frac{dn_0 \sin \theta}{dn_s}$ denotes the bulk responsivity of the structure.

Two major sources of noise in the system are camera noise (including dark noise and shot noise) and laser power fluctuation. Therefore, camera noise, laser power fluctuation and total noise level are investigated individually. The camera is set to low read noise mode and records 719 frames per second with an ROI of 30 pixels \times 30 pixels. The dark noise was first assessed with 25,000 frames. The laser power fluctuation was measured over 25,000 frames. The total noise level was measured with the incident angle tuned to half height of the resonance of TE mode where the maximum of slope and sensitivity is over 25,000 frames. Data recordings are conducted with the same camera. $\frac{dI}{dn_0 \sin \theta}$, which is the maximum slope of reflectivity of the TE structure, is set to 1030.6 as measured in the system and $\frac{dn_0 \sin \theta}{dn_s}$, which is the responsivity of the structure, is $0.8598 RIU^{-1}$.

Noise specification of the camera is the hard limit on the sensitivity of the designed system. As we are building a compact system with limited space, the camera used is a 16-bit sCMOS camera with passive cooling. The standard deviation of the normalized dark noise measured is 7.5037×10^{-8} which corresponds to a noise-equivalent sensitivity of $8.5728 \times 10^{-11} RIU$. The dark noise situation can

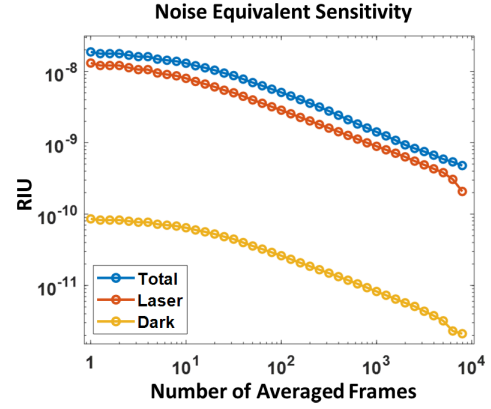


Fig. 8. Noise-equivalent RIU (sensitivity) measured respectively from the laser, the camera and entire system.

be further improved by averaging frames or using a camera with active cooling.

Laser power fluctuation is the main source of noise in the system, as it pervades the whole system. The laser power fluctuation is measured with a silver mirror temporarily mounted after the beam expansion lens pair pivoting the beam into the camera directly. The standard deviation of normalized noise from laser power is 1.146×10^{-5} which corresponds to a noise-equivalent sensitivity of $1.308 \times 10^{-8} RIU$. Averaging $\sim 10^4$ frames, the noise-equivalent sensitivity could be limited to $\sim 10^{-10} RIU$.

Combining these noise sources, without frame averaging, the system can achieve a sensitivity of $1.874 \times 10^{-8} RIU$. As shown in Fig. 8(a), averaging 794 frames (~ 1 s acquisition time) further improves the sensitivity to $1.609 \times 10^{-9} RIU$. Although the averaging makes a considerable improvement to the signal-to-noise ratio, the improvement is less rapid than expected for entirely random samples, which is attributed to a degree of correlation between successive frames. The sensitivity is obtained without any attempt to compensate for laser fluctuation, which can be achieved using a reference beam that does not interact with the sample. Phase detection or polarization detection are also expected to give substantial improvements with the same structure [3], [26], [27].

The short-term stability of the structure is addressed in the noise analysis where the small value of the minimum detectable RIU is evidence that the sample is stable in the short term. In terms of repeatability and long-term stability, three batches of samples have been manufactured and different samples and different regions on the same sample were measured and consistent FoM values within 10% were obtained, and the experiment of TE samples was repeated over a couple of weeks, and it was noted that the FoM did not vary by more than 5%.

IV. CONCLUSION

We have theoretically and experimentally demonstrated a high aspect-ratio open grating based Fabry-Perot resonance structures with both TM and TE polarizations for high-FoM

refractive index measurement. Theoretically, transmission line model and Smith chart have been utilized to give an intuition on layer-wise physical mechanism and separated analysis on responsivity from in-grating and out-grating. Experimentally, Table III shows a direct comparison among results from conventional SPR, TM and TE samples. An FoM of 1394 is achieved with TE samples with 34% duty cycle, which is a 44-fold improvement over conventional SPR. A 10-fold improvement over conventional SPR in FoM is achieved with TM samples with 23% duty cycle. As shown in Fig. 1(b), the samples have a $1\mu\text{m}$ -thick grating layer. The difference between experiments and simulations is a result of additional Cr layer and errors in the grating profile. In the simulation, with TE polarization, even a uniform-thick layer instead of the grating layer has a FoM of 376. In the designed system of the TE mode, noise-equivalent sensitivity of $1.874 \times 10^{-8} RIU$ is observed without frame averaging. With 794 frames averaging (taking ~ 1 second acquisition time), the noise-equivalent sensitivity is further improved to $1.609 \times 10^{-9} RIU$.

EBL has been used in the process to provide more freedom in sample dimensions. However, when mass-manufacturing commercial sensors, as the grating dimensions are fixed, nano-imprinting lithography technique will be a better tool since it greatly reduces fabrication cost and hugely improve performance consistency across different batches of samples. For applications in acidic or alkaline conditions, an extra protective coating of Parylene or Cytop would be desired. Alternatively, more durable materials such as PDMS could be employed with nanoimprinting to further improve sample lifetime, however, this may not be necessary for single use applications.

High FoM of 1394 is observed in the experiments, and there is still room for further improvements of the FoM as this is still less than the simulated values. The aspect ratio used is 5:1, and as mentioned in Ref. [28], it is practical for PMMA to achieve an aspect ratio of 10:1. The increased aspect ratio increases bulk responsivity and FoM. Various improvement approaches will be developed and applied in our future work since the structure also exhibits extraordinary performance and bulk responsivity potential at telecom optical wavelength of SCL-band for spectroscopy. High-FoM feature could allow this structure to be used in wide range of applications e.g. kinetic molecule binding [29], multichannel refractive index sensing [30] and photoacoustic sensors [31].

APPENDIX A

TYPICAL ACQUIRED IMAGE SEQUENCE FROM THE SYSTEM

Each pixel on the camera should ideally correspond to light at the same incident angle. The sequence in Fig. 9 shows the images on the camera as the incident angle is changed by increments of 0.02° , with low intensities around image 20. The angular response of the sensors was obtained by averaging a region of 20 by 20 pixels.

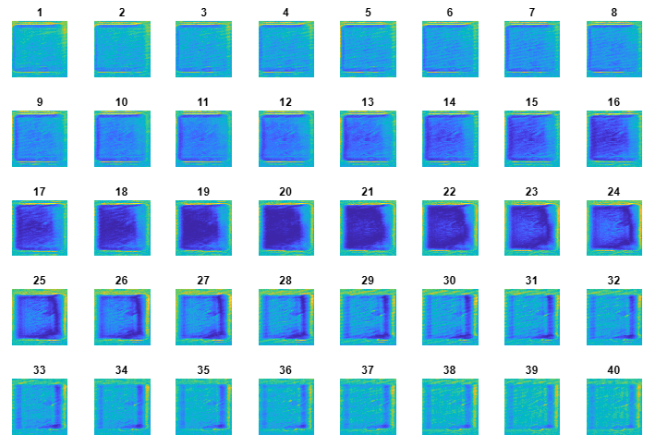


Fig. 9. A typical acquired image sequence covering a mode of TM polarization with 0.02° angular increments between each frame.

APPENDIX B

SAMPLE PREPARATION PROCEDURE

The structure was fabricated by sputtering and electron beam lithography. The substrate of the structure was N-BK7 coverslip, with refractive of 1.515 at 633nm. The coverslips were ultrasonic cleaned with acetone and IPA for 5 minutes each and rinsed with water for 2 minutes, then sputtered with chromium and gold. The chromium layer was deposited from RF gun with a power of 100W for 20 seconds yielding a thickness of 2nm. The gold layer was deposited from a DC gun with a power of 100W yielding a deposition rate of 0.44 nm per second. The designed thicknesses for TM samples and TE samples are 48 nm and 38 nm respectively. It should be noted that the thickness of the gold layer was verified by the surface profiler for each batch of sputtered sample to ensure optimum operation. And the simulation shows an error of 1-second sputtering time (0.44 nm) in thickness makes no more than 1.5% in the FoM.

Prior to deposition of e-Beam resist, Adhesion Promoter (AP) 300-80 (Allresist GmbH) was spin-coated for 1 minute at 4000rpm. This layer is crucial for high aspect-ratio structures since it enhances the affinity between the gold layer and PMMA layer and prevent the grating from falling off during the development process. AR-P 672.08 positive PMMA e-Beam resist (Allresist GmbH) was chosen as the EBL resist used for its high aspect ratio, high resolution and contrast properties and good adhesion to glass and metal. The chosen resist also gives required thickness of $1\mu\text{m}$ and high aspect ratio up to 10. The e-Beam resist is then spin-coated onto the samples at 3000rpm for a thickness of $1\mu\text{m}$ and the samples are pre-baked for 3 minutes at 150°C on hot plate. The manufactured grating has a period of 600 nm and duty cycles of 23% and 42% for TM samples in order to compare the effect of duty cycles and 35% for TE samples. The resist is exposed for writing with EBP 5150 (Raith BV) with a voltage of 100kV and a current of 5nA. Prior to large area writing, the dose is determined by dose test from 500 mC/cm^2 to 1500 mC/cm^2 . 850 mC/cm^2 was chosen for optimized grating profile and accurate linewidth. After the exposure, the sample

was then developed in AR 600-56 consisted of 1 MIBK and 3 IPA for 2 minutes and 15 seconds followed by immersion in AR 600-60 (IPA) for 1 minute for stopping. Afterwards the sample was transferred into DI water to dissolve the residual developer and resist. Then, the sample was post-baked for 1 minute at 130° on a hot plate to strengthen the structure.

ACKNOWLEDGMENT

The authors would like to thank the Photonics Center of Shenzhen University for fabrication support and the Instrumental Analysis Center of Shenzhen University for analytical support. Xiaoping Jiang would like to thank the Hong Kong Polytechnic University for his studentship.

REFERENCES

- [1] M. A. Ettabib *et al.*, "Waveguide enhanced Raman spectroscopy for biosensing: A review," *ACS Sensors*, vol. 6, no. 6, pp. 2025–2045, Jun. 2021.
- [2] W. Liu *et al.*, "Surface plasmon resonance chemical sensor composed of a microstructured optical fiber for the detection of an ultra-wide refractive index range and gas-liquid pollutants," *Opt. Exp.*, vol. 29, no. 25, pp. 40734–40747, Dec. 2021.
- [3] J. Wang *et al.*, "Highly sensitive multipoint real-time kinetic detection of surface plasmon bioanalytes with custom CMOS cameras," *Biosensors Bioelectron.*, vol. 58, pp. 157–164, Aug. 2014.
- [4] C. Chung, Y.-K. Kim, D. Shin, S.-R. Ryoo, B. H. Hong, and A.-H. Min, "Biomedical applications of graphene and graphene oxide," *Accounts Chem. Res.*, vol. 46, no. 10, pp. 2211–2224, Oct. 2013.
- [5] F. Vollmer and L. Yang, "Label-free detection with high-Q microcavities: A review of biosensing mechanisms for integrated devices," *Nanophotonics*, vol. 1, nos. 3–4, pp. 267–291, 2012.
- [6] M. Piliarik, H. Sipova, P. Kvasnicka, N. Galler, J. R. Krenn, and J. Homola, "High-resolution biosensor based on localized surface plasmons," *Opt. Exp.*, vol. 20, no. 1, pp. 672–680, Jan. 2012.
- [7] M. Piliarik, M. Vala, I. Tichý, and J. Homola, "Compact and low-cost biosensor based on novel approach to spectroscopy of surface plasmons," *Biosensors Bioelectron.*, vol. 24, no. 12, pp. 3430–3435, Aug. 2009.
- [8] Y. Sun and X. Fan, "Optical ring resonators for biochemical and chemical sensing," *Anal. Bioanal. Chem.*, vol. 399, no. 1, pp. 205–211, Jan. 2011.
- [9] J. T. Robinson, L. Chen, and M. Lipson, "On-chip gas detection in silicon optical microcavities," *Opt. Exp.*, vol. 16, no. 6, pp. 4296–4301, Mar. 2008.
- [10] M. Shen and M. G. Somekh, "A general description of the performance of surface plasmon sensors using a transmission line resonant circuit model," *IEEE Sensors J.*, vol. 19, no. 23, pp. 11281–11288, Dec. 2019.
- [11] J.-Y. Jing, Q. Wang, W.-M. Zhao, and B.-T. Wang, "Long-range surface plasmon resonance and its sensing applications: A review," *Opt. Lasers Eng.*, vol. 112, pp. 103–118, Jan. 2019.
- [12] E. Gonzalez-Valencia, I. D. Villar, and P. Torres, "Novel Bloch wave excitation platform based on few-layer photonic crystal deposited on D-shaped optical fiber," *Sci. Rep.*, vol. 11, no. 1, p. 11266, Dec. 2021.
- [13] R. Caroselli *et al.*, "Experimental study of the sensitivity of a porous silicon ring resonator sensor using continuous in-flow measurements," *Opt. Exp.*, vol. 25, no. 25, pp. 31651–31659, Dec. 2017.
- [14] M. Li, R. Singh, C. Marques, B. Zhang, and S. Kumar, "2D material assisted SMF-MCF-MMF-SMF based LSPR sensor for creatinine detection," *Opt. Exp.*, vol. 29, no. 23, pp. 38150–38167, Aug. 2021.
- [15] A. K. Sharma and C. Marques, "Design and performance perspectives on fiber optic sensors with plasmonic nanostructures and gratings: A review," *IEEE Sensors J.*, vol. 19, no. 17, pp. 7168–7178, Sep. 2019.
- [16] L. Singh *et al.*, "Gold nanoparticles and uricase functionalized tapered fiber sensor for uric acid detection," *IEEE Sensors J.*, vol. 20, no. 1, pp. 219–226, Jan. 2020.
- [17] Z. Wang, R. Singh, C. Marques, R. Jha, B. Zhang, and S. Kumar, "Taper-in-taper fiber structure-based LSPR sensor for alanine aminotransferase detection," *Opt. Exp.*, vol. 29, no. 26, pp. 43793–43810, Dec. 2021.
- [18] S. Sasivimolkul, S. Pechprasarn, and M. G. Somekh, "Analysis of open grating-based Fabry–Pérot resonance structures with potential applications for ultrasensitive refractive index sensing," *IEEE Sensors J.*, vol. 21, no. 9, pp. 10628–10636, May 2021.
- [19] Y. Xu *et al.*, "Optical refractive index sensors with plasmonic and photonic structures: Promising and inconvenient truth," *J. Lightw. Technol.*, vol. 7, no. 9, May 2019, Art. no. 1801433.
- [20] P. Lalanne, J. P. Hugonin, and P. Chavel, "Optical properties of deep lamellar gratings: A coupled Bloch-mode insight," *J. Lightw. Technol.*, vol. 24, no. 6, pp. 2442–2449, Jun. 2006.
- [21] A. Polemi and K. L. Shuford, "Transmission line equivalent circuit model applied to a plasmonic grating nanosurface for light trapping," *Opt. Exp.*, vol. 20, no. S1, pp. A141–A156, Jan. 2012.
- [22] O. Levy and D. Stroud, "Maxwell Garnett theory for mixtures of anisotropic inclusions: Application to conducting polymers," *Phys. Rev. B, Condens. Matter*, vol. 56, no. 13, pp. 8035–8046, Oct. 1997.
- [23] T. Liu, Y. Pang, M. Zhu, and S. Kobayashi, "Microporous Co@CoO nanoparticles with superior microwave absorption properties," *Nanoscale*, vol. 6, no. 4, pp. 2447–2454, 2014.
- [24] GE Healthcare, *Biacore Sensor Surface Handbook BR-1005-71 Edition AB*. Accessed: Apr. 1, 2022. [Online]. Available: <https://timothyspringer.org/files/tas/files/biacore3000-sensorsurface.pdf>
- [25] A. Savitzky and M. J. E. Golay, "Smoothing and differentiation of data by simplified least squares procedures," *Anal. Chem.*, vol. 36, no. 8, pp. 1627–1639, Jul. 1964.
- [26] S. G. Nelson, K. S. Johnston, and S. S. Yee, "High sensitivity surface plasmon resonance sensor based on phase detection," *Sens. Actuators B, Chem.*, vol. 35, nos. 1–3, pp. 187–191, Sep. 1996.
- [27] M. Shen, Q. Zou, X. Jiang, F. Feng, and M. G. Somekh, "Single-shot three-input phase retrieval for quantitative back focal plane measurement," *Photon. Res.*, vol. 10, no. 2, pp. 491–502, Feb. 2022.
- [28] M. J. Rooks, E. Kratschmer, R. Viswanathan, J. Katine, R. E. Fontana, and S. A. MacDonald, "Low stress development of poly(methylmethacrylate) for high aspect ratio structures," *J. Vac. Sci. Technol. B, Microelectron.*, vol. 20, no. 6, pp. 2937–2941, Nov./Dec. 2002.
- [29] H. Altug, S.-H. Oh, S. A. Maier, and J. Homola, "Advances and applications of nanophotonic biosensors," *Nature Nanotechnol.*, vol. 17, no. 1, pp. 5–16, Jan. 2022.
- [30] D. Wang *et al.*, "Real-time multi-channel SPR sensing based on DMD-enabled angular interrogation," *Opt. Exp.*, vol. 26, no. 19, pp. 24627–24636, Sep. 2018.
- [31] W. Song *et al.*, "Isometrically resolved photoacoustic microscopy based on broadband surface plasmon resonance ultrasound sensing," *ACS Appl. Mater. Interfaces*, vol. 11, no. 30, pp. 27378–27385, Jul. 2019.



Xiaoping Jiang received the B.Sc. degree from the Beijing Institute of Technology in 2016. He is now pursuing the Ph.D. degree with Hong Kong Polytechnic University. He is also a Research Assistant with the Nanophotonics Research Centre, Shenzhen University. His research interests include optical sensors and photoacoustics.



Mengqi Shen received the Ph.D. degree from the University of Nottingham in 2018. After a period of working as a Research Assistant with Hong Kong Polytechnic University, she joined Shenzhen University as a Postdoctoral Researcher. Her research interests include imaging, sensors, measurement, and detectors.



Daniel Pak-Kong Lun (Senior Member, IEEE) received the B.Sc. (Hons.) degree from the University of Essex, U.K., in 1988, and the Ph.D. degree from The Hong Kong Polytechnic University in 1991. In 1991, he joined The Hong Kong Polytechnic University as a Research Associate, where he is now an Associate Professor and the Associate Head of the Department of Electronic and Information Engineering. His research interests include wavelets theory, signal and image enhancement, computational imaging, and deep neural networks. He is currently an Associate Editor of IEEE SIGNAL PROCESSING LETTERS and IEEE OPEN JOURNAL OF CIRCUITS AND SYSTEMS.



Michael G. Somekh received the degree in metallurgy and science of materials from Oxford University and the Ph.D. degree in microwave electronics from Lancaster University, U.K. After research fellowships at Oxford University, his first academic position was with University College London. Then, he joined the University of Nottingham, Nottingham, U.K., where he founded the Applied Optics Group. After a period working in Hong Kong, he joined Shenzhen University as a Distinguished Professor and also holds a part-time position at Nottingham University as a Professor of Optical Engineering. His research interests include imaging, sensors, and ultrasonics. He is a Fellow of the Institute of Physics and was elected as a Fellow of the Royal Academy of Engineering (the U.K. National Engineering Academy) in 2012 in recognition of his interdisciplinary work.



Wen Chen (Senior Member, IEEE) received the Ph.D. degree from the National University of Singapore. He conducted extensive research as a Research Associate in 2010 and a Research Fellow with the National University of Singapore from 2011 to 2015. He was a Visiting Scholar at Harvard University in 2013. He joined The Hong Kong Polytechnic University as an Assistant Professor in December 2015. Since July 2021, Dr. Chen has been an Associate Professor with the Department of Electronic and Information

Engineering, Photonics Research Institute, The Hong Kong Polytechnic University. He has authored or coauthored more than 130 international journals and conference papers on his field of specialization. He is listed among the top 2% of the world's most highly cited scientists by Stanford University. His research interests include computational optics, information photonics, optical imaging, optical encoding, optical sensing, free-space optical data transmission, and deep learning in optics and photonics. He serves as an Associate Editor for several academic journals (e.g., *Optics and Lasers in Engineering* and *Optics Express*).